

# Behavior of active filaments near solid-boundary under linear shear flow

Shalabh K. Anand\* and Sunil P. Singh†

Department of Physics,  
Indian Institute of Science Education and Research,  
Bhopal 462 066, Madhya Pradesh, India

The steady-state behavior of dilute suspension of self-propelled filament confined between planar walls subjected to the Couette-flow is reported herein. The effect of hydrodynamics has been taken into account using a mesoscale simulation approach. We present positional and angular probability distributions of filament with varying propulsive force and shear-flow. Distribution of centre-of-mass of the filament shows adsorption near the surfaces, which diminishes with the flow. The excess density of the filament decreases with Weissenberg number as  $Wi^{-\beta}$  with  $\beta \approx 0.8$ , in the intermediate shear limit. The orientational moment also decreases near the wall as  $Wi^{-\delta}$  with  $\delta \approx 1/5$ , this variation is relatively slower than the bulk. Orientational moment near the wall shows strong dependence on the propulsive force and it varies as  $Pe^{-1/3}$  for large  $Pe \geq 1$ . The active filament shows orientational preference with flow near the surfaces, which splits into upstream and downstream swimming. The population splitting from a unimodal (propulsive force dominated regime) to bimodal phase (shear dominated regime) is also identified here.

## I. INTRODUCTION

The abundance of swimmers is widespread in nature, from microscopic to macroscopic length scales such as, algae[1, 2], bacteria[3, 4], spermatozoa[5–7], *C. elegans*, fishes, etc. The self-propulsion helps them in endurance of getting food, avoiding various chemical toxins, in reaching to female reproductive egg, and for several other biological processes in active complex environments. Typically, motile organisms live near walls, which make them vulnerable to any external perturbations especially a fluid-flow[8, 9]. The interplay between propulsive force and a fluid-flow induced motility is referred in the literature as rheotaxis. Understanding behavior of self-propelled organisms near a surface is crucial from several bio-applications point of view to a fundamental quest[10].

Microswimmers play a fervent role in life processes therefore their dynamics and structure are subject of immense interest in research[11–30]. The artificial swimmers can be mimicked as a potential model system for targeted delivery in the pharmaceutical applications[31–33]. The influence of weak external perturbations on the microswimmers not only lead to significant scale structural and population change[34–36], but it can also make them motile against the stream near surfaces[34–44]. The mechanisms behind the upstream motility are attributed in terms of shear-induced orientation, active stresses, reduction in local viscosity, and inhomogeneous hydrodynamic drag [11, 45, 46].

In living matter, swimming against the flow is very common, particularly for the fishes[47], *C. elegans*[29], *E. Coli*, sperms [30], etc. The main difference in the mechanism of swimming at two different length-scales is the intervention of visual and tactile sensory

cues[47, 48] at macroscopic scales, while the motion is driven by the interplay of various physical interactions for microswimmers[49].

In an attempt to understand dynamics of microswimmers near the surfaces, simpler yet effective models have been proposed in the literatures as elongated shape swimmers[24, 34–36, 41–44, 50–52]. Despite their simplicity in nature, they are able to capture complex behaviors such as, surface accumulation, [20, 53, 54], upstream swimming,[34–36], and flow induced angular alignment[55], etc. The population splitting from a unimodal to a bimodal phase is obtained in terms of chirality and its angular speed[56]. The upstream motion can be tuned in the visco-elastic fluid [57]. The propulsion mechanism changes accumulation and angular alignment on the walls. More specifically a puller orthogonally points towards the wall, whereas pushers and neutral swimmers tend to align along the wall[58]. The external flow leads to reduction in the adsorption of the active dimer like swimmers on the surfaces[35].

In this article, we attempt to provide an understanding of a slender-like motile object near the solid interface under flow. The weakening of accumulation and angular distribution near the surfaces will be addressed in elaborate manner. In the previous studies, the long-range correlation among solvents and its interactions with swimmers and solid-boundaries were absent[34, 36]. To complete the model, hydrodynamics is included for detailed study of the dilute suspension of self-propelled filaments. The hydrodynamic interactions can induce effective attractive interaction between wall and an elongated shape swimmer[54, 59, 60], which is crucial to be considered in such studies.

We consider a simulation model that incorporates an explicit solvent based mesoscale approach known as multi-particle collision dynamics (MPC)[61–63] clubbed with molecular-dynamics (MD). The dilute suspension of filaments result enhancement in average density near a solid-boundary with increase in Péclet number, while

\* skanand@iiserb.ac.in

† spsingh@iiserb.ac.in

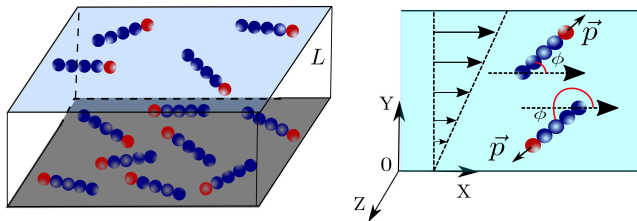


FIG. 1. A schematic diagram of active filaments confined between walls. Bottom wall is in grey and top wall is shown in light blue for visibility. A red bead in the front head of swimmers shows their polarity. Arrow in the right diagram displays the direction of flow.

fluid flow leads to desorption of the swimmers. This is addressed in terms of the short time diffusion, alignment of a rod-like swimmer across the channel, and residence time near wall and bulk. The hydrodynamic interactions increase the adsorption in weak flow regime. The swimmers align (anti-align) parallel to the flow at top (bottom) wall. The shear-induced alignment exhibits a non-monotonic behavior on increasing flow rate, which is attributed as blindness of polarity at higher flow. The number of majority and minority populations at walls display orientation-switching. In shear dominant regime, population splits from unimodal to bimodal phase. We have obtained the orientational moment near the surfaces which shows a power law variation with an exponent slightly smaller than found in the bulk limit. In addition to that it also shows a power law scaling with Péclet number.

The organisation of the paper is as follows: In section 2, simulation methodology of the self-propelled filaments and the fluid has been discussed. Results are presented in section 3, with discussion of the outcome of the competition among flow, confinement and active forces. In the last section results are summarised.

## II. MODEL

In this section, we present simulation method adopted for active filaments in solution. At first, modelling of the active filament is presented, and subsequently implementation of a coarse-grained model for the solvent is introduced. A schematic display of the system confined along y-direction is shown in Fig. 1. In the other two spatial directions (x and z), periodic boundary condition is applied.

### A. Active Filament

We consider  $N_p$  filaments, where each filament consists a linear sequence of  $N$  monomeric units, connected via spring and bending potentials. Thus total  $N_t = N \times N_p$  number of monomers are present in the solution. An

excluded volume interaction among the monomers and walls are also taken into account. The total potential energy of a filament is written as  $U = U_{sp} + U_b + U_{LJ} + U_w$ . Here  $U_{sp}$ ,  $U_b$ ,  $U_w$ , and  $U_{LJ}$  are harmonic, bending, wall and repulsive part of the Lennard-Jones(LJ) potentials, respectively. The harmonic and bending potentials for  $j^{th}$  filament is given as,

$$U_{sp}^j + U_b^j = \frac{k_s}{2} \sum_{i=1}^{N-1} (|\mathbf{R}_i| - l_0)^2 + \frac{\kappa}{2} \sum_{i=1}^{N-2} (\mathbf{R}_{i+1} - \mathbf{R}_i)^2, \quad (1)$$

where  $l_0$  is the equilibrium bond length,  $R_i$  is the length of the  $i^{th}$  bond vector,  $R_i = |\mathbf{r}_{i+1} - \mathbf{r}_i|$  with  $\mathbf{r}_i$  to be position vector of the  $i^{th}$  monomer,  $k_s$  and  $\kappa$  are spring constant and bending rigidity of the filament, respectively.

The excluded volume potential,  $U_{LJ}$  is modelled as repulsive part of Lennard-Jones potential for shorter distance, i.e.,  $R_{ij} < 2^{1/6}\sigma$ , among all monomers,

$$U_{LJ} = \sum_{i=1}^{N_t-1} \sum_{j=i+1}^{N_t} 4\epsilon \left[ \left( \frac{\sigma}{R_{ij}} \right)^{12} - \left( \frac{\sigma}{R_{ij}} \right)^6 + \frac{1}{4} \right], \quad (2)$$

and for  $R_{ij} \geq 2^{1/6}\sigma$ , it is treated as  $U_{LJ} = 0$ . Here,  $\epsilon$  and  $\sigma$  are the LJ interaction energy and the diameter, respectively. Interactions between wall and monomers  $U_w$  are also treated same as given in above Eq. 2, to constrain filaments within wall premises. A monomer feels the repulsive force from a boundary wall when it reaches within the distance  $2^{1/6}\sigma/2$  from the wall.

Self-propulsion is achieved by imposing tangential force along each bond vector of  $i^{th}$  filament in the form given as  $F_a^i = \sum_{j=1}^{N-1} f_a \hat{t}(\mathbf{R}_j)$  [64, 65],  $f_a$  and  $\hat{t}(\mathbf{R}_j)$  reads as the strength of the active force, and  $j^{th}$  tangent vector.

### B. MPC fluid

The MPC method is also known as stochastic rotation dynamics approach [61–63, 66, 67], here solvent molecules are treated as point particles of mass  $m$ . Their dynamics consist of streaming followed by collision in the alternating steps. In the streaming step, solvent particles move ballistically with their respective velocities, and their positions are updated according to the following rule,  $\mathbf{r}_i(t+h) = \mathbf{r}_i(t) + h\mathbf{v}_i(t)$ , where  $h$  is the MPC collision time-step for  $i = 1, 2, 3, \dots, N_s$ . In the collision step, solvent molecules are sorted into cubic cells of side  $a$  and their relative velocities, concerning the centre-of-mass velocity of the cell, are rotated around a randomly oriented axis by an angle  $\alpha$ . The particle velocities are then updated as

$$\mathbf{v}_i(t+h) = \mathbf{v}_{cm}(t) + \Omega(\alpha)(\mathbf{v}_i(t) - \mathbf{v}_{cm}), \quad (3)$$

where  $\mathbf{v}_{cm}$  is the centre-of-mass velocity of the cell of  $i^{th}$  particle, and  $\Omega(\alpha)$  stands for the rotation operator. During collision, all solvent molecules within a cell interact

with each other in a coarse-grained fashion by colliding at the same time such that the momentum remains conserved, which ensures the long-range spatial and temporal correlations among the solvent molecules that results hydrodynamic interactions.

A solvent molecule's velocity is reversed by bounce-back rule as  $\mathbf{v}_i = -\mathbf{v}_i$ [68–70] when it crosses a wall, which imposes no-slip boundary on the surfaces. The interaction of the MPC-fluid and filament monomers are incorporated during the collision step. Here, momentum of monomers in the calculation of centre-of-mass velocity of the cell is included during the collision step[71, 72].

Furthermore, an active force on the filament adds momentum in the polarity direction of a filament, which destroys the local momentum conservation. To insure local momentum conservation, the same force to the solvent particles are imposed in opposite direction to only those cells where filament monomers are present during each collision step[54]. The presence of propulsive force and flow continuously increases energy of the system, which may lead to rise in the temperature of fluid. A cell level canonical thermostat known as Maxwell-Boltzmann scaling[73, 74] is incorporated to remove the excess energy and keep the desired temperature of the system. A random shift of the collision cell at every step is also performed to avoid the violation of Galilean invariance[67, 75].

A linear fluid-velocity ( $v_x = \dot{\gamma}y$ ) profile along the x-axis is generated by moving the wall at  $y = L_y$ (top wall in the Fig.1) at constant speed ( $v_x = \dot{\gamma}L_y$ ). The equations of motion of solvent molecules are modified in the vicinity of wall[70, 76, 77]. The velocity of a solvent relative to the surface is reversed with bounce-back rule in the streaming step when it touches a wall, which again ensures no-slip boundary conditions on the walls. During the solvent-wall interaction, a moving wall transfers momentum to the solvent molecules which drives a linear profile on average along the x-direction. In addition to that, virtual particles with the velocity taken from a Maxwell-Boltzmann distribution with mean equal to wall velocity are added in the partially filled cells[73, 74].

### C. Simulation Parameters

All the physical parameters are scaled in terms of the MPC cell length  $a$ , mass of a fluid particle  $m$ , thermal energy  $k_B T$  and time  $\tau = \sqrt{ma^2/k_B T}$ . The size of simulation box are taken here as ( $L_x = 80, L_y = 50, L_z = 25$ ) with periodic boundary conditions in x and z spatial directions, and solid walls are in y-directions at 0 and  $L_y$ . Other parameters are chosen as spring constant  $k_s = 1000k_B T/l_0^2$ , stiffness parameter  $\kappa = 5000k_B T/l_0^2$ ,  $l_0/a = \sigma/a = 1$  and  $\epsilon/k_B T = 1$ . Unless explicitly mentioned, number of monomers in a filament is considered to be  $N = 10$ , and number of such filaments in the system is considered as 50, which is a dilute concentration of monomer in solution as  $\rho_m = 0.005a^{-3}$ , and number

density of rod is  $\rho_p = 0.0005a^{-3}$ , which is well below the isotropic-nematic transition[78]. The velocity-Verlet algorithm is used for the integration of equations of motion for active polymers, and integration time-step is chosen to be  $h_m = 0.01\tau$ . The strength of active force is measured in terms of a dimensionless quantity called Péclet number, which is defined as  $Pe = \frac{f_a \sigma}{k_B T}$ .

For the MPC fluid, collision time-step is taken as  $h = 0.05\tau$ , rotation angle  $\alpha = 130^\circ$ , average number of fluid particles per cell  $\langle N_c \rangle = 10$ . These parameters correspond to the transport coefficient of the fluid as zero-shear viscosity  $\eta_s \equiv 17\sqrt{mk_B T}/a^2$ . The strength of flow is expressed in terms of a dimensionless Weissenberg number  $Wi$  defined as  $Wi = \dot{\gamma}\tau_r$ , where  $\tau_r$  is the polymer's relaxation time. Here,  $Wi$  is a measure of the flow strength over the thermal fluctuations, in the limit of  $Wi \leq 1$ , thermal fluctuations dominate. However for  $Wi \geq 1$ , flow plays a significant role. All the simulations are performed in the range of  $0 \leq Wi \leq 150$  and  $0 \leq Pe \leq 3$ . For each data set, 50 independent runs has been generated for better statistics. Our simulations always correspond for the Reynolds number ( $Re$ ) bounded by the range of  $Re < 0.1$ .

## III. RESULTS

In our model, an active filament is polar and it moves along one of its end. Therefore, it can align along the surfaces, which leads to adsorption on the surfaces and depletion in bulk[20, 53]. The fluid-flow weakens the adsorption and leads to homogeneity for a dimer like molecule[35]. An active filament may preferentially align parallel or anti-parallel to the flow direction. Here, we unravel the influence of linear shear-flow on a dilute suspension of active filaments in a confined channel. We present the influence of flow on surface adsorption, average local orientation profile, population of upstream swimmers near the wall and importance of hydrodynamic interactions on swimmers.

### A. Surface accumulation

First, we address results in the absence of flow. The distribution of passive filaments are shown in Fig. 2-a at  $Wi = 0$  as a function of distance from the bottom wall  $y' = y/L_y$ , where walls are present at  $y' = 0$  (bottom) and  $y' = 1$  (top). The probability distribution  $P(y')$  is uniform due to translational entropy, which favours homogeneity. Near the surfaces ( $|L_y - y| \leq l/2$ ), it reflects depletion due to exclusion of the filament from the steric repulsion of the filament. As expected,  $P(y')$  of the active filament increases with the speed of the swimmers (see Fig.2-a) near the surfaces. The normalised distribution of swimmers near the surfaces reflect large inhomogeneity specifically in the limit of large  $Pe$ . This is consistent with the previous findings[20, 35, 53]. The distribution

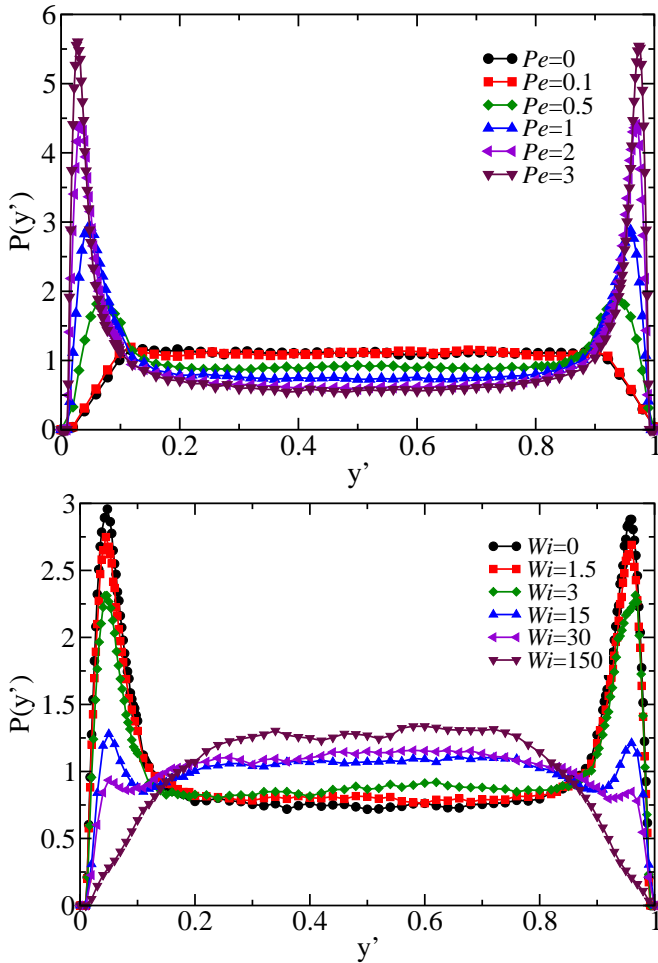


FIG. 2. The probability distribution of rod as a function of channel height ( $y' = y/L_y$ ). a) Shows for  $Wi = 0$  for various  $Pe$ , and b) displays for  $Pe = 1$  various flow-rates, where  $L_y$  is the channel width.

function has peaks near the walls in the limit of large Péclet numbers, which confirms the adsorption of swimmers on the solid boundaries.

The motility induced adsorption is understood in terms of combination of active force, steric repulsion, and drag. Large active force results into longer persistence motion and rapid movement through out the channel, which eventually leads to the surfaces at a shorter time. Once they reach nearby the surface, they align and move along the surface. The large drag perpendicular to the filament axis causes them to reside near the wall for much longer compare to the bulk, which results into higher probability density with  $Pe$ . This will also be vetted in terms of short time diffusion across channel.

The shear disrupts the concentration of filaments on the surfaces, which is reflected in probability density in Fig. 2-b for a given  $Pe = 1$  for a range of  $Wi$ . The activity induced surface adsorption for  $Wi = 0$  (without flow) shows maximum density as it has highest peak near the surface. The peak diminishes with increase in the fluid-

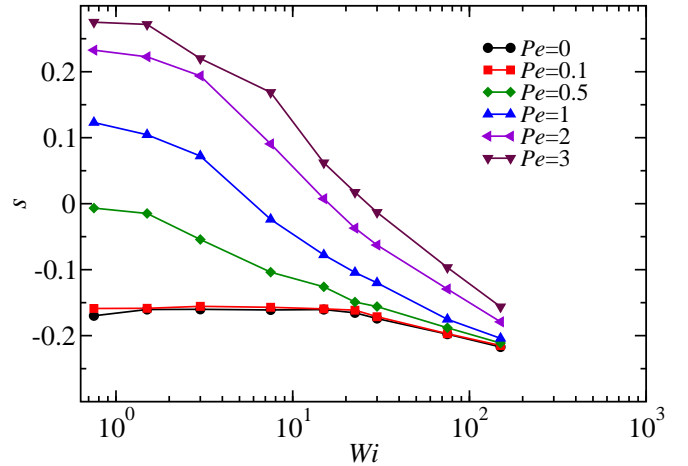


FIG. 3. Surface excess as a function of flow-rate  $Wi$  for various  $Pe$  as shown in figure.

flow for  $Wi > 1$ , and it disappears nearly at  $Wi \sim 30$ . The distribution becomes homogeneous along the channel( see Fig. 2-b) with low concentration of swimmers near the surface. In the limit of  $Wi > 100$ , density of rods near the surface is very small compared to the bulk density. Interestingly, this is similar to the equilibrium distribution (for  $Pe = 0$  at  $Wi=0$ ) in Fig. 2-a.

The desorption driven by the flow can be justified in terms of the orientational alignment of the polar filament, tumbling motion, and suppression of diffusion across the channel. An active filament aligns along flow direction, which breaks the rotational symmetry of swimmers causing less number of filaments aligned towards a wall. Consequently, the probability of a filament on the wall decreases. The accumulation close to the wall is severely influenced by the shear induced orientational alignment. The flow can act as a control variable for the adsorption of polar filaments at the wall.

To quantify the depletion driven by the flow, we estimate surface excess from the probability distribution of the filament as[54]

$$s = \int_0^{l/2} [P(y) - P_b] dy, \quad (4)$$

where  $s$  is measurement of the excess surface density near the surface relative to bulk and  $P_b$  is read as bulk distribution. The definition of  $s$  is constructed in a way that it becomes unity for full adsorption, whereas in case of uniform distribution it is zero. Smaller density from the bulk will result negative surface excess as in the case of passive filament.

For slow swimming speed,  $Pe < 1$ , probability density is smaller than the bulk, thus the surface excess is negative. It increases with  $Pe$  and becomes positive for  $Pe > 1$  (see Fig. 3). The variation in  $s$  with flow strength  $Wi$  in the limit of  $Pe < 1$  is negligible, which reaches to a significant change for larger Péclet number  $Pe > 1$  as Fig. 3 illustrates. The change in  $s$  grows with  $Pe$  as

a function of Wiessenberg number. At sufficiently high value of  $Wi$ , surface excess becomes negative suggesting the weakening of localisation at the walls. Desorption of filament in the large  $Wi$  suggests the dominance of shear over active forces.

The qualitative behavior of a surface adsorption can also be accessed from the scaling arguments. In this approach, trajectory of a swimmer is treated as a semiflexible polymer[54] with persistence length of trajectory defined as  $\xi_p = v/D_r$ , where  $v$  and  $D_r$  are the average speed of the filament and the rotational diffusion coefficient, respectively. Furthermore, under a linear shear-flow, rotational diffusion can be approximated in the form of tumbling time as[79, 80]

$$D_r \approx \frac{k_B T}{\eta_s l^3} (1 + cWi^{-2/3})^{-1}, \quad (5)$$

where  $c$  is some constant. We present analysis in two extreme limits. In the limit of  $Wi \ll 1$ ,  $D_r$  is unperturbed by fluid-flow, whereas for  $Wi \gg 1$ ,  $D_r$  will vary as  $Wi^{-2/3}$ .

The probability of finding a filament in the vicinity of thickness  $l/2$  from a wall is given as  $p = \tau_w / (\tau_w + \tau_b) = 1 / (1 + \tau_b / \tau_w)$ , with  $\tau_w$  to be the residence time of a filament at the wall and  $\tau_b$  to be the residence time in bulk. In order to estimate  $\tau_w$ , we take  $x_f$  to be the distance travelled along the surface. It is simply  $x_f = vt$  and  $y$  is normal distance of filament from the closest wall, then  $y = x_f^{3/2} / \xi_p^{1/2}$  and at  $y = l/2$ , time is  $t = \tau_w$ . Following the same approach as derived in Ref. [54] for the active filaments, we have extended the scaling approach under linear shear-flow. Therefore, the residence time  $\tau_w$  can be expressed as,

$$\tau_w \sim \frac{1}{v} \left( \frac{l^2 \xi_p}{4} \right)^{1/3} = \left( \frac{l^2 v^{-2}}{4D_r} \right)^{1/3}. \quad (6)$$

In our case, the persistence length  $\xi_p > L_y/2$  for all  $Pe$ , thus we approximate the  $\tau_b$  calculation in diffusive regime. Approximating  $\tau_b$  in diffusive regime[54],  $\tau_b$  can be written as,

$$\tau_b \sim \frac{L_y}{v_b} \left( \frac{l}{\xi_p} \right)^{1/3} = \frac{L_y}{v_b} \left( \frac{lD_r}{v} \right)^{1/3}, \quad (7)$$

with  $v = Pe/\gamma + a_2 Wi$  and  $v_b = Pe/\gamma$ , where  $\gamma$  is friction coefficient. Combining expression Eq. 6 and 7,

$$\tau_w / \tau_b \sim \frac{v_b}{L_y} \left( \frac{lv^{-1}}{4D_r^2} \right)^{1/3}. \quad (8)$$

In the limit of  $Wi \ll 1$ , the ratio varies as  $\tau_w / \tau_b \sim v^{2/3}$ , which recovers the results proposed by Elgeti *et al*[54]. In the limit of  $Wi \gg 1$ ,  $\tau_w / \tau_b \sim Wi^{-\beta}$  with  $\beta = 7/9$ . In this limit, the probability of finding a filament near the wall also becomes  $p \sim Wi^{-\beta}$ . Thus one can approximate surface excess in the large shear limit as,

$$s = \frac{pL_y - l}{L_y - l} \sim \frac{a_0 Wi^{-\beta} - l}{L_y - l}. \quad (9)$$

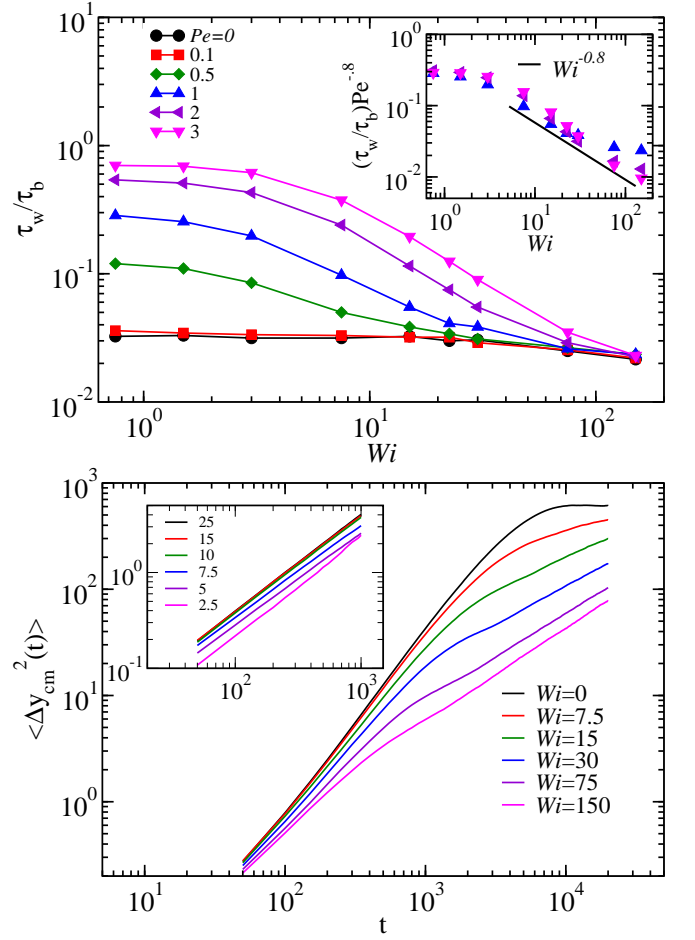


FIG. 4. a) Ratio of residence time of the active filament near the surface with the bulk as a function of  $Wi$  for various  $Pe$ . Inset shows the scaled curve of  $(\tau_b/\tau_w)Pe^{-0.8}$  in range of  $Pe \geq 1$ . b) The MSD of centre-of-mass of filament for various  $Wi$  at a given  $Pe = 2$ . Inset shows the MSD for different distances from the wall of the channel.

Furthermore, for  $Wi \gg 1$ ,  $Wi^{-\beta} \rightarrow 0$ , leading to saturation at  $s = -l/(L_y - l)$ . In the intermediate limit  $Wi > 1$ ,  $s$  decrease as a power law  $s \sim Wi^{-\beta}$ , with an exponent  $\beta \sim 0.8$ , as shown in Fig3-a.

## B. Residence time and Diffusion

To clarify the effect of shear on surface adsorption, we estimate residence time of the filament near the wall and in the bulk. The time spend by a filament in the neighbourhood of the wall with constraint that once it aligns along the wall is addressed as residence time  $\tau_w$  on the wall. Similarly, the average time spent in the bulk is computed as twice of the time taken by a filament starting from the centre of channel to either of the surfaces in the vicinity of  $l/2$ . The ratio of residence times is displayed in Fig.4-a as a function of  $Wi$  for various  $Pe$ . As we can see from Fig.4-a, the qualitative behavior is similar in

nature as surface excess (see Fig.3). The ratio decreases with the flow and increases with  $Pe$ . Our results follows the relation  $\tau_w/\tau_b \sim Pe^{0.8}$  for small  $Wi$ , the exponent is slightly larger than the scaling predictions as obtained in Eq.8. The influence of shear is also displayed here as  $\tau_w/\tau_b \sim Wi^{-\beta}$  with  $\beta \approx 0.8$  in the intermediate limit of  $Wi$  for  $Pe > 1$ . The same exponent is also obtained from scaling behavior in Eq.8. The weak flow has negligible influence on  $\tau_w/\tau_b$ . On the other hand, stronger flow (for  $Pe > 1$ ) can lead to strong change in  $\tau_w/\tau_b$  (see Fig.4-a). The influence of active forces are weak in the case of  $Pe < 1$ , therefore shear has negligible influence on  $\tau_w/\tau_b$  thus the adsorption is independent of shear flow. This also establishes influence of activity and flow rate on the accumulation of swimmers.

Furthermore, in the limit of  $Wi \gg 1$ ,  $\tau_w/\tau_b$  saturates to a slightly smaller number than the passive case. This is associated with the alignment of filaments along the flow leading to transport via transverse diffusion across the channel. Hence diffusive motion results constant  $\tau_w/\tau_b$  irrespective of presence of flow and propulsive forces.

We quantify influence of surface and flow on short time diffusion across the channel. The role of flow on the mean-square-displacement(MSD) of the centre-of-mass of the filament along the gradient direction at  $Pe = 2$  for various  $Wi$  is displayed in Fig.4-b. For  $Wi = 0$ , the MSD shows super-diffusive regime in short time succeeded by a saturation in long time limit. The saturation occurs due to presence of wall, which is nearly at half-width of the channel. The flow strength of  $Wi > 1$ , aligns filament along x-axis thus the super-diffusive regime is suppressed relatively to shorter time. The diffusive behavior appears at shorter time scales as shown in Fig.4-b. The short time diffusion of the filaments across the channel at sufficiently higher shear-rate explains the lower density of the filament on the surfaces. The flow aligns them thus suppress the ballistic movement of filaments in the gradient direction, consequently reduction in density occurs on both surfaces.

The diffusion nearby surfaces is also influenced by hydrodynamic interactions. This is assessed in a more intricate fashion in terms of the short time MSD across the channel with separation from the surface. Inset of Fig.4-b displays the MSD for various distances from the wall at  $Pe = 0$  and  $Wi = 0$ . The short time MSD is nearly independent in the bulk. The short time MSD is sufficiently small in the vicinity of the surface compared to that in the bulk. The decrease in the short time diffusion occurs due to alignment along the surface, which forces them to diffuses perpendicular to their axis. This exhibits higher drag and leads to smaller MSD. The inhomogeneous drag due to hydrodynamic interactions contributes in slow translational and rotational diffusion.

Despite the decrease in absolute value of residence time[54] with propulsive force, surface adsorption grows. This is addressed here as follows, if a filament's polarity in bulk is pointing upwards then it reaches to the top wall and if it is aligned downward then it may reach to the bot-

tom wall. The time required to reach on a surface drastically reduces with propulsive force, results in enhancement of the probability of collision with walls. This is clearly demonstrated in Fig. 4-a as ratio of  $\tau_w/\tau_b$ . Therefore, adsorption on the surfaces increases even though the residence  $\tau_w$  time decays with  $Pe$ . With increase in  $Wi$ , angular alignment leads to the decrease in the ratio. As a consequence, decrease in surface excess is also addressed in terms of MSD across the channel in Fig.4-b. We can conclude here that the flow diminishes the length of persistence motion across the channel which can be enhanced by the propulsive force.

### C. Flow Induced Alignment

Now we embark on the quantification of flow induced orientation of active filaments particularly near the surfaces, which enables the quantification of direction of a swimmer. For this we compute two different kind of angles, one is the angle between the projection of unit vector  $\vec{p}$  (tail-to-head as shown in Fig1) on the flow-gradient plane and flow direction and later one is the angle between  $\vec{p}$  and flow direction. The former one is azimuthal angle used in the characterisation of the shear-induced alignment of a polymer[80, 81], and the later one is used in the identifying upstream and downstream swimming behavior[34, 35].

At first, we analyse variation of orientational moment along the flow direction defined as  $\chi_p = 1 - p_x p_x$ , as a function of  $Wi$  and  $Pe$  in the bulk (inset) and close to the wall as displayed in Fig.5-a. Swimmers are oriented randomly in all possible ways in the bulk at low  $Wi$ , they align along the flow direction for higher  $Wi$ . The variation of the alignment in the bulk shows a power law behavior as  $Wi^{-\delta}$  with  $\delta = 1/3$ [82–85]. Note that the scaling exponent is nearly independent of propulsive force as qualitative behavior is shown from a solid line in inset of Fig.5-a. In the neighbourhood of solid-boundaries, swimmers are more aligned along the flow due to propulsive and excluded volume forces. The angle decreases with increase in  $Pe$ . Thus,  $\chi_p$  shows slower variation with  $Wi$  for large  $Pe \geq 1$ , therefore it results to a smaller exponent. This is reflected in the exponent as  $\delta \sim 1/5$  for all  $Pe \geq 1$ . Interestingly, the angular alignment also shows variation as  $\chi_p \sim Pe^{-1/3}$ , near the wall. As shown in Fig5-a, a universal curve for all  $Pe \geq 1$  is obtained by scaling with  $Pe^{1/3}$ . This suggests that the orientational moment decreases as  $\chi_p \sim Pe^{-1/3}$  for all  $Wi$ . In the large shear limit, it varies as  $\chi_p \sim Wi^{-1/5}$  for  $Pe \geq 1$ .

In the case two, we quantify the angle between tail-to-head vector and flow direction as shown in Fig.1. In our convention, if a filament's orientation angle lies in the range of  $-\pi/2 \leq \phi \leq \pi/2$  then it is termed as downstream swimmer, similarly, if this is between  $\pi/2 \leq \phi \leq 3\pi/2$  then it is referred as upstream swimmer. The profile for various  $Wi$  ( see Fig.5-b) is shown across the channel for  $Pe = 0.5$ . A filament does not have any preferred

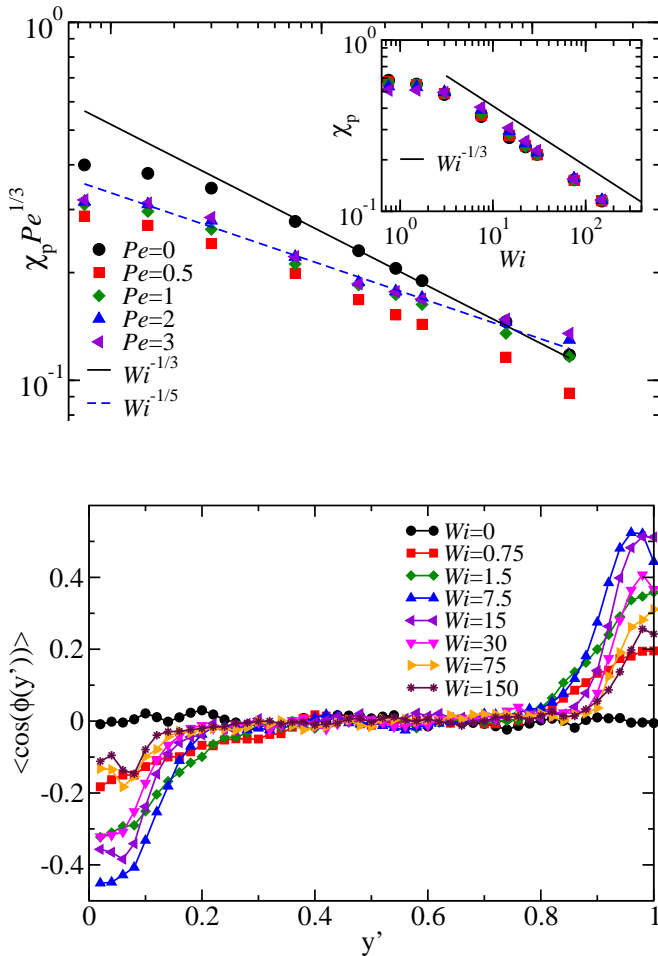


FIG. 5. a) Orientation moment  $\chi_p$  in the vicinity of the wall, it follows power law relation as  $Wi^{-1/5}$  (dashed line) for  $Pe > 1$  and solid line shows.  $Wi^{-1/3}$  for  $Pe = 0$ . Inset shows a universal curve for the  $\chi_p$  in the bulk for all  $Pe$ . Solid line shows power law variation with exponent  $1/3$ . b) Average orientation profile of active filaments as a function of channel height ( $y' = y/L_y$ ) from the bottom wall for  $Pe = 0.5$  for various  $Wi$ .

direction for  $Wi = 0$ , thus  $\langle \cos(\phi(y')) \rangle \approx 0$  throughout the channel. This signifies movement of swimmer is rotationally symmetric for  $Wi = 0$ .

For non-zero  $Wi$ , symmetry is broken therefore  $\langle \cos(\phi(y')) \rangle$  displays a non-zero value. A positive value corresponds to the downstream swimming in the upper halves ( $y' \geq 0.5$ ) and a negative value for upstream in the lower halves ( $y' \leq 0.5$ ). The average alignment of the system grows with the flow as Fig. 5-b exhibits a peak near the top wall and a depth near the bottom wall. Height of the peak grows with  $Wi$  and reaches to a maximum value, which goes down with further increase in  $Wi$  as reflected in Fig. 5-b for  $Wi > 30$  at  $Pe = 0.5$ . In addition to decrease in height of the peak, width of the distribution also gets narrower towards the surface. This illustrates the flow driven localisation of the upstream and downstream swimming in vicinity of the surfaces.

The average preference of swimmers to be upstream or downstream diminishes as we go far from the surface. This can be visualised in terms of distribution of angle  $\phi$  in the shear-gradient plane. Figure 6 displays a colormap to show the angle distribution ( $P(\phi)$ ) along the channel  $y' = y/L_y$  for various values of  $Wi$  at  $Pe = 3$ . Figures have peaks at  $\phi = 0$  and  $\pi$ , they correspond to localisation of downstream and upstream, respectively near the walls, with presence of single dominant phase for small  $Wi$ . In the limit of large  $Wi$ , both halves exhibit symmetric distribution around  $0$  and  $\pi$ , leading to symmetric orientations all over the channel displaying bimodal phase.

We now turn our attention to the flow driven angular distribution of the filament in close vicinity of the walls ( $\Delta y = l/2$ ). As expected, the angle distribution  $P(\phi)$  near the top wall is symmetric about  $\pi/2$ , which consists two identical peaks centred at  $\phi = 0$ , and  $\phi = \pi$  at  $Wi = 0$  (see Fig.7-a). This displays the distribution of angle at a fixed  $Pe = 0.5$  for several values of  $Wi$ . The peak height at  $\phi = 0$  (major) increases and  $\phi = \pi$  (minor) decreases with  $Wi$ . The height of peak shows a decrease followed by increase with  $Wi$  at  $\pi$ .

Summarising above results here, the active filaments align themselves along (against) the flow direction at the top(bottom) wall assisted by the torque due to shear-force in the Péclet number dominant regime as shown in Fig. 7-b. However, in the shear dominant regime, i.e  $Wi/Pe > 5$ , filament aligns also against (along) the flow at the top (bottom) surface. The shear-induced alignment is identified here as a critical point which provides the turning point of the peak at  $\phi = \pi$  from decrease to increase.

#### D. Population of filament at surface

We address here population of the upstream and downstream swimmers specially near the surfaces. The coupling between torque due to flow and the propulsive force leads the downstream to be the majority population and upstream to be the minority population near the top wall (see for Fig.7). Figure8-a displays the fraction of majority population ( $\rho_{mj} = N_{mj}/N_p$ ) with respect to total population at  $y = L_y$ , here  $N_{mj}$  is number of filaments aligned along flow. The fraction  $\rho_{mj}$  grows in small shear limit for all  $Pe$ . The initial increase is followed by reduction in the fraction in the limit of  $Wi/Pe > 5$ , which continues to decrease with  $Wi$ . The flow assists alignment, as a consequence of that majority population increases in the limit of  $Wi/Pe < 5$ . In the limit of large shear, the fast tumbling motion leads to an increase in the effective rotational diffusion. As a result, the alignment against the flow also increases which causes decline in the majority population and increase in the minority population.

The magnitude of shear force required to shrink the majority population for higher activity strength is sub-

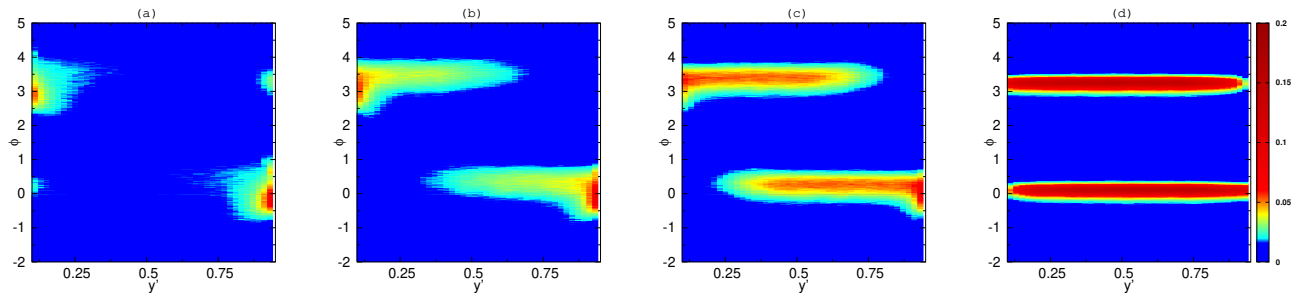


FIG. 6. The distribution of angle  $\phi$  made by the filaments as a function of channel width for a)  $Wi = 3$ , b)  $Wi = 7.5$ , c)  $Wi = 15$ , and d)  $Wi = 150$  at  $Pe = 3$ .

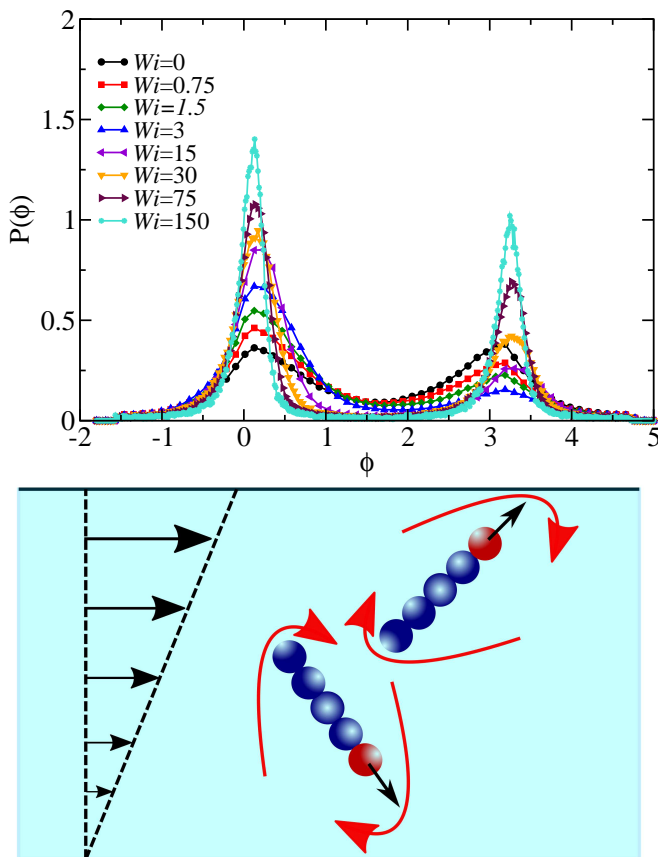


FIG. 7. a) The variation of  $\phi$  near the top wall  $y' = 1$  for  $Pe = 0.5$  for various  $Wi = 0, 0.75, 1.5, 7.5, 30, 75$  and  $150$ . b) Schematics of flow induced alignment of filaments on the top and bottom half of the channel.

stantially large, as we can see that location of peak shifts towards higher  $Wi$  (see Fig. 8-a). The minority fraction,  $\rho_{mn} = N_{mn}/N$ , at the top wall displays the same trend as shown in inset of Fig.8-a. Here population decrease is succeeded by increase for all  $Pe$ . The behavior is same for both surfaces. The difference in the preference of orientation at the top and bottom surfaces is due to clockwise torque on the filament, as shown in Fig.7, which favours

downstream on the top wall and upstream on the bottom wall.

Thus we have identified here three regimes for a given magnitude of  $Pe$ : i) At small  $Wi$ , where swimming speed  $Pe$  plays the sole role. ii) Intermediate regime, where both forces compete with each other. In this regime, increase in majority population is followed by its decrease. iii) At sufficiently high  $Wi$ , shear plays the major role hence the effect of activity is diminished, and therefore it behaves like a passive filament with equal population.

Based on the above summary, we have identified a phase-diagram in Fig. 8-b in  $Pe$  and  $Wi$  parameter space for the switching of orientation profile at the walls. Here the critical value of  $Wi$  has been displayed as onset of green shaded area as a function of  $Pe$ . The gradient in color reflects the ratio of minority to majority population. The green shaded region shows the inception of population splitting phenomenon at a given  $Pe$ , region below the shaded area is the majority population dominated. Although fraction of majority population may be higher above the shaded region, but their population has started declining with flow. The critical value of Weissenberg number shifts towards larger value with Péclet number. The population splitting phenomenon occurs in the range of  $Wi/Pe > 5$ . Thus in shear dominant regime, swimmers do upstream and downstream swimming with equal weight throughout the channel.

### E. Effect of hydrodynamics

In this section, we compare the role of hydrodynamic correlations on the structure of confined active filaments. For this, we have performed simulations with the random MPC which exhibits similar background solvent, except absence of long-range correlations among solvents[86–88]. The comparison of the surface adsorption with and without HI are demonstrated in Fig. 9 for same  $Pe$ , which suggests that the adsorption is enhanced with hydrodynamics in case of weak shear. The inset illustrates the distribution of swimmers as a function of distance from the wall, which clearly shows a substantial difference in accumulation with and without HI. The role of flow on surface

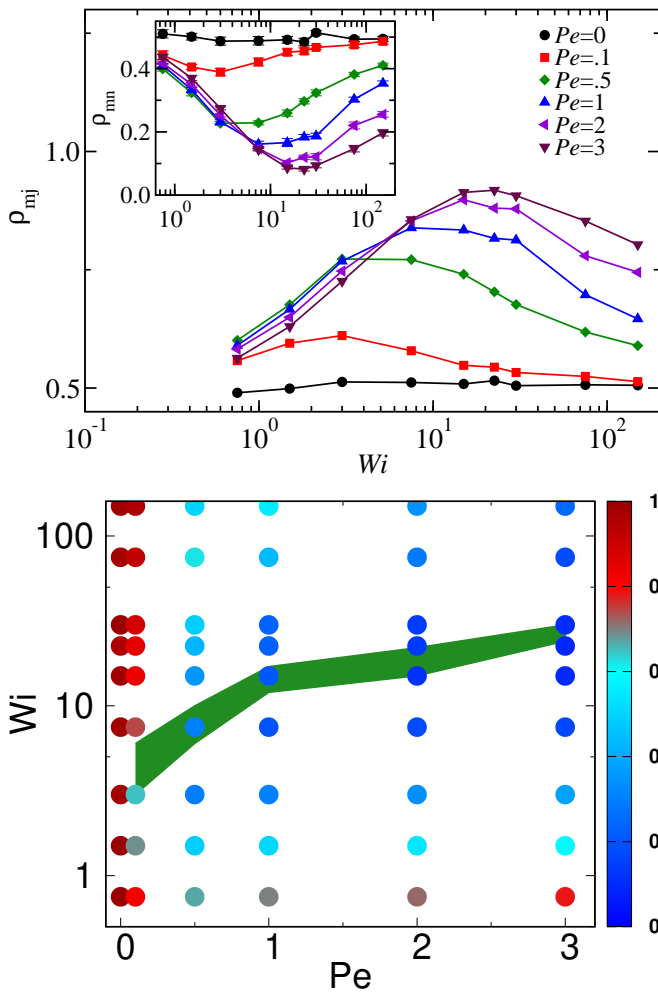


FIG. 8. a) Number density of majority population parallel to the flow at top wall. Inset shows the fraction of minority population of downstream to the total population rods at the top wall. b) Phase diagram showing the critical value of  $Pe$ , where minority population of swimmers at the wall start increasing. Colour bar is based on the magnitude of ratio of minority to majority.

excess is also shown in Fig.9, which is higher with hydrodynamics for small  $Wi$ . The enhancement in the adsorption with HI occurs due to increase in inhomogeneous drag force and interaction of solvents with wall[46, 89]. Another important aspect needs to be mentioned here that in the intermediate shear-rate the difference in surface excess diminishes. In this limit, transport due to transverse diffusive motion is dominant thus a swimmer moves across the channel relatively slower due to small transverse diffusion with HI for smaller filaments, which gives smaller surface excess.

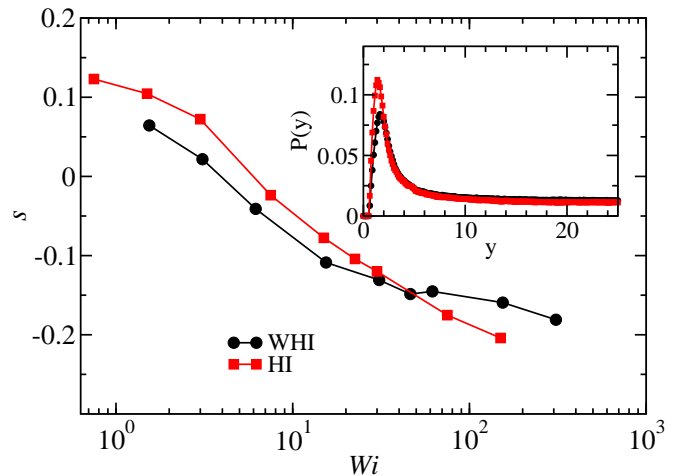


FIG. 9. Comparison of surface excess of the filament with (squares) and without (bullets) HI at  $Pe = 1$ . Inset shows the distribution of rods as a function of distance from the wall at  $Wi = 0$  for  $Pe = 1$ .

#### IV. SUMMARY AND CONCLUSION

In summary, we have presented dynamics of dilute concentration of active filaments confined between parallel walls under linear shear flow using a hybrid MD-MPC simulations. Active filaments display strong tendency to accumulate on the wall with propulsive forces, and shear flow weakens the adsorption. The adsorption and desorption are analysed in terms of alignment across the channel, anisotropic friction of the filament, MSD across the channel, collision with wall, and residence time. The filament gets aligned near the surfaces and anisotropic nature of friction[14, 90] results slow short time translational and rotational diffusion across the channel, which causes relatively larger residence time near the wall, hence higher adsorption without flow. Similarly, shear induced angular alignment [70, 80, 91] suppresses the ballistic motion across the channel leading to small concentration.

The adsorption is quantified in terms of surface excess "s", we have shown that it follows a power-law behavior as  $s \sim Wi^{-\beta}$ , with  $\beta \approx .8$  in the intermediate regime of flow. The simulation results are validated with help of scaling theory, which predicts nearly same exponent  $\beta = 7/9$ . It behaves like a passive system with weak adsorption on the surfaces with even smaller surface excess than the passive case for  $Wi \gg 1$ . The adsorption and desorption is understood with help of residence time near the wall and bulk  $\tau_w/\tau_b$ , which captures the same dependence. The suppression of angular fluctuations causes slow decrease in the bulk residence thus adsorption decreases with shear.

The active filaments choose their polar alignment along the flow, the angular distribution shows a non-monotonic profile at the walls with  $Wi$ . The increase in angular alignment of upstream(downstream) particles at bot-

tom(top) wall is followed by the onset of its decrease after a critical shear-rate. In addition to that, the fraction of majority (upstream) population at the top wall also shows a non-monotonic increase followed by decrease with  $Wi$ . The local angular distributions near the surfaces lead to a power law variation as,  $\chi_p \sim Wi^{-\delta}$  with exponent  $\delta \sim 1/5$ , smaller than the bulk suggesting weaker relative variation. More importantly, we found that the orientational moment decreases with propulsive force near the wall unlike the bulk where it is independent of the Péclet number. The dependence of  $\chi_p$  is associated with the steep steric interactions with walls.

The critical shear rate for the onset of the splitting of the unimodal to bimodal behavior, varies nearly linear with  $Pe$ . This separates two different regimes, where population splits from unimodal to bimodal or vice-versa with increasing (decreasing) shear-rates. Inception of

population splitting shows the weakening of effect of activity in the regime of higher shear forces eventually leading to equal population with angular separations at  $\pi$  and  $0$ [34]. The dynamics of modelled swimmers in complex active environments would be interesting to consider in the future studies, this may bring closer to more realistic systems. More-specifically, different geometry of surfaces, shear-gradients, chiral shape of swimmers, run and tumble motion of swimmers, and viscoelastic media may lead to several distinguishable motional phases.

## V. ACKNOWLEDGEMENTS

Authors acknowledge HPC facility at IISER Bhopal for computation time. We thank DST SERB Grant No. YSS/2015/000230 for the financial support. SKA thanks IISER Bhopal for the funding.

- 
- [1] D. L. Ringo, *The Journal of Cell Biology* **33**, 543 (1967), ISSN 0021-9525.
  - [2] M. Polin, I. Tuval, K. Drescher, J. P. Gollub, and R. E. Goldstein, *Science* **325**, 487 (2009), ISSN 0036-8075.
  - [3] D. F. Blair, *Annual Review of Microbiology* **49**, 489 (1995), pMID: 8561469.
  - [4] H. C. BERG, *Nature* **245**, 380 (1973).
  - [5] J. GRAY, *Journal of Experimental Biology* **32**, 775 (1955), ISSN 0022-0949.
  - [6] W. Shack, C. Fray, and T. Lardner, *Bulletin of Mathematical Biology* **36**, 555 (1974), ISSN 0092-8240.
  - [7] D. Woolley, *Reproduction* **126**, 259 (2003).
  - [8] C.-k. Tung, F. Ardon, A. G. Fiore, S. S. Suarez, and M. Wu, *Lab Chip* **14**, 1348 (2014).
  - [9] E. Lauga and T. R. Powers, *Reports on Progress in Physics* **72**, 096601 (2009).
  - [10] W. Gao, D. Kagan, O. S. Pak, C. Clawson, S. Campuzano, E. Chuluun-Erdene, E. Shipton, E. E. Fullerton, L. Zhang, E. Lauga, et al., *small* **8**, 460 (2012).
  - [11] A. P. Berke, L. Turner, H. C. Berg, and E. Lauga, *Phys. Rev. Lett.* **101**, 038102 (2008).
  - [12] B. Sabass and U. Seifert, *Phys. Rev. Lett.* **105**, 218103 (2010).
  - [13] K. Schaar, A. Zöttl, and H. Stark, *Phys. Rev. Lett.* **115**, 038101 (2015).
  - [14] J. Elgeti and G. Gompper, *EPL (Europhysics Letters)* **109**, 58003 (2015).
  - [15] M. Tournus, A. Kirshtein, L. Berlyand, and I. S. Aranson, *Journal of the Royal Society Interface* **12**, 20140904 (2015).
  - [16] S. Das, G. Gompper, and R. G. Winkler, *New Journal of Physics* **20**, 015001 (2018).
  - [17] W. Uspal, M. N. Popescu, S. Dietrich, and M. Tasinkevych, *Soft Matter* **11**, 6613 (2015).
  - [18] A. Daddi-Moussa-Ider, M. Lisicki, C. Hoell, and H. Löwen, *The Journal of chemical physics* **148**, 134904 (2018).
  - [19] R. Ledesma-Aguilar, H. Löwen, and J. M. Yeomans, *The European Physical Journal E* **35**, 70 (2012).
  - [20] J. Elgeti and G. Gompper, *The European Physical Journal Special Topics* **225**, 2333 (2016), ISSN 1951-6401.
  - [21] M. Potomkin, A. Kaiser, L. Berlyand, and I. Aranson, *New Journal of Physics* **19**, 115005 (2017).
  - [22] T. Omori and T. Ishikawa, *Physical Review E* **93**, 032402 (2016).
  - [23] Y.-G. Tao and R. Kapral, *Soft Matter* **6**, 756 (2010).
  - [24] J. de Graaf, A. J. Mathijssen, M. Fabritius, H. Menke, C. Holm, and T. N. Shendruk, *Soft Matter* **12**, 4704 (2016).
  - [25] I. Pagonabarraga and I. Llopis, *Soft Matter* **9**, 7174 (2013).
  - [26] L. Zhang, T. Petit, Y. Lu, B. E. Kratochvil, K. E. Peyer, R. Pei, J. Lou, and B. J. Nelson, *ACS Nano* **4**, 6228 (2010), pMID: 20873764.
  - [27] J. Hill, O. Kalkanci, J. L. McMurphy, and H. Koser, *Phys. Rev. Lett.* **98**, 068101 (2007).
  - [28] T. Kaya and H. Koser, *Biophysical Journal* **102**, 1514 (2012), ISSN 0006-3495.
  - [29] J. Yuan, D. M. Raizen, and H. H. Bau, *Proceedings of the National Academy of Sciences* **112**, 3606 (2015), ISSN 0027-8424.
  - [30] V. Kantsler, J. Dunkel, M. Blayney, and R. E. Goldstein, *Elife* **3**, e02403 (2014).
  - [31] J. R. Howse, R. A. L. Jones, A. J. Ryan, T. Gough, R. Vafabakhsh, and R. Golestanian, *Phys. Rev. Lett.* **99**, 048102 (2007).
  - [32] W. F. Paxton, S. Sundararajan, T. E. Mallouk, and A. Sen, *Angewandte Chemie International Edition* **45**, 5420 (2006), ISSN 1521-3773.
  - [33] J. Palacci, S. Sacanna, A. Abramian, J. Barral, K. Hanson, A. Y. Grosberg, D. J. Pine, and P. M. Chaikin, *Science advances* **1**, e1400214 (2015).
  - [34] H. Nili, M. Kheyri, J. Abazari, A. Fahimniya, and A. Naji, *Soft Matter* **13**, 4494 (2017).
  - [35] S. Chilukuri, C. H. Collins, and P. T. Underhill, *Journal of Physics: Condensed Matter* **26**, 115101 (2014).
  - [36] B. Ezhilan and D. Saintillan, *Journal of Fluid Mechanics* **777**, 482522 (2015).

- [37] Bretherton and Rothschild, Proceedings of the Royal Society of London B: Biological Sciences **153**, 490 (1961), ISSN 0080-4649.
- [38] Z. Zhang, J. Liu, J. Meriano, C. Ru, S. Xie, J. Luo, and Y. Sun, Scientific Reports **6**, 23553 EP (2016), article.
- [39] J. Katuri, W. E. Uspal, J. Simmchen, A. Miguel-López, and S. Sánchez, Science advances **4**, eaao1755 (2018).
- [40] R. Rosengarten, A. Klein-Struckmeier, and H. Kirchhoff, Journal of bacteriology **170**, 989 (1988).
- [41] K. Son, D. R. Brumley, and R. Stocker, Nature Reviews Microbiology **13**, 761 (2015).
- [42] R. Rusconi, J. S. Guasto, and R. Stocker, Nature physics **10**, 212 (2014).
- [43] T. Kaya and H. Koser, Physical review letters **103**, 138103 (2009).
- [44] Y. Meng, Y. Li, C. D. Galvani, G. Hao, J. N. Turner, T. J. Burr, and H. Hoch, Journal of Bacteriology **187**, 5560 (2005).
- [45] G. Li and J. X. Tang, Phys. Rev. Lett. **103**, 078101 (2009).
- [46] B. Lin, J. Yu, and S. A. Rice, Physical Review E **62**, 3909 (2000).
- [47] J. C. Montgomery, C. F. Baker, and A. G. Carton, Nature **389**, 960 EP (1997).
- [48] A. G. P., Biological Reviews **49**, 515 (1974).
- [49] Marcos, H. C. Fu, T. R. Powers, and R. Stocker, **109**, 4780 (2012), ISSN 0027-8424.
- [50] A. Najafi and R. Golestanian, Physical Review E **69**, 062901 (2004).
- [51] J. Pande and A.-S. Smith, Soft Matter **11**, 2364 (2015).
- [52] S. Babel, H. Löwen, and A. M. Menzel, EPL (Europhysics Letters) **113**, 58003 (2016).
- [53] J. Elgeti and G. Gompper, EPL **101**, 48003 (2013).
- [54] Elgeti, J. and Gompper, G., EPL **85**, 38002 (2009).
- [55] C.-k. Tung, F. Ardon, A. Roy, D. L. Koch, S. S. Suarez, and M. Wu, Phys. Rev. Lett. **114**, 108102 (2015).
- [56] H. Nili, Scientific Reports **8**, 8328 (2018).
- [57] A. J. T. M. Mathijssen, T. N. Shendruk, J. M. Yeomans, and A. Doostmohammadi, Phys. Rev. Lett. **116**, 028104 (2016).
- [58] P. Magaretti and H. Stark, The Journal of Chemical Physics **146**, 174901 (2017).
- [59] T. Pedley and J. Kessler, Annual Review of Fluid Mechanics **24**, 313 (1992).
- [60] A. P. Berke, L. Turner, H. C. Berg, and E. Lauga, Physical Review Letters **101**, 038102 (2008).
- [61] A. Malevanets and R. Kapral, The Journal of Chemical Physics **110**, 8605 (1999).
- [62] R. Kapral, *Multiparticle Collision Dynamics: Simulation of Complex Systems on Mesoscales* (John Wiley and Sons, Inc., 2008), pp. 89–146, ISBN 9780470371572.
- [63] G. Gompper, T. Ihle, D. M. Kroll, and R. G. Winkler, *Multi-Particle Collision Dynamics: A Particle-Based Mesoscale Simulation Approach to the Hydrodynamics of Complex Fluids* (Springer Berlin Heidelberg, Berlin, Heidelberg, 2009), pp. 1–87, ISBN 978-3-540-87706-6.
- [64] R. E. Isele-Holder, J. Elgeti, and G. Gompper, Soft matter **11**, 7181 (2015).
- [65] S. K. Anand and S. P. Singh, Physical Review E **98**, 042501 (2018).
- [66] A. Malevanets and R. Kapral, The Journal of Chemical Physics **112**, 7260 (2000).
- [67] T. Ihle and D. M. Kroll, Phys. Rev. E **63**, 020201 (2001).
- [68] A. Lamura, G. Gompper, T. Ihle, and D. Kroll, EPL (Europhysics Letters) **56**, 319 (2001).
- [69] A. Lamura and G. Gompper, The European Physical Journal E **9**, 477 (2002).
- [70] S. P. Singh and M. Muthukumar, The Journal of chemical physics **141**, 09B610\_1 (2014).
- [71] A. Malevanets and J. M. Yeomans, EPL (Europhysics Letters) **52**, 231 (2000).
- [72] M. Ripoll, K. Mussawisade, R. G. Winkler, and G. Gompper, EPL (Europhysics Letters) **68**, 106 (2004).
- [73] C. Huang, A. Chatterji, G. Sutmann, G. Gompper, and R. Winkler, Journal of Computational Physics **229**, 168 (2010), ISSN 0021-9991.
- [74] C.-C. Huang, A. Varghese, G. Gompper, and R. G. Winkler, Phys. Rev. E **91**, 013310 (2015).
- [75] T. Ihle and D. M. Kroll, Phys. Rev. E **67**, 066705 (2003).
- [76] R. G. Winkler and C.-C. Huang, The Journal of Chemical Physics **130**, 074907 (2009).
- [77] J. K. Whitmer and E. Luijten, Journal of Physics: Condensed Matter **22**, 104106 (2010).
- [78] P.-G. de Gennes and J. Prost, *The physics of liquid crystals*, vol. 83 (Oxford university press, 1995).
- [79] R. G. Winkler, Physical review letters **97**, 128301 (2006).
- [80] C.-C. Huang, R. G. Winkler, G. Sutmann, and G. Gompper, Macromolecules **43**, 10107 (2010).
- [81] C.-C. Huang, G. Gompper, and R. G. Winkler, Journal of Physics: Condensed Matter **24**, 284131 (2012).
- [82] J. Park and J. E. Butler, Journal of Fluid Mechanics **630**, 267 (2009).
- [83] M. Rahnama, D. L. Koch, and E. S. Shaqfeh, Physics of Fluids **7**, 487 (1995).
- [84] S. B. Chen and D. L. Koch, Physics of Fluids **8**, 2792 (1996).
- [85] L. Leal and E. Hinch, Journal of Fluid Mechanics **46**, 685 (1971).
- [86] N. Kikuchi, A. Gent, and J. Yeomans, The European Physical Journal E **9**, 63 (2002).
- [87] N. Kikuchi, C. Pooley, J. Ryder, and J. Yeomans, The Journal of chemical physics **119**, 6388 (2003).
- [88] M. Ripoll, R. Winkler, and G. Gompper, The European Physical Journal E **23**, 349 (2007).
- [89] J. Padding and W. J. Briels, The Journal of chemical physics **132**, 054511 (2010).
- [90] M. Doi and S. F. Edwards, *The theory of polymer dynamics*, vol. 73 (oxford university press, 1988).
- [91] S. P. Singh, A. Chatterji, G. Gompper, and R. G. Winkler, Macromolecules **46**, 8026 (2013).